Journal of Applied Geophysics 121 (2015) 116–127

Contents lists available at ScienceDirect

Journal of Applied Geophysics

journal homepage: www.elsevier.com/locate/jappgeo

The Total Component (or vector magnitude) and the Energy Envelope as tools to interpret airborne electromagnetic data: A comparative study

Jacques K. Desmarais [a,*], Richard S. Smith [b]

[a] Earth Sciences, University of Saskatchewan, 114 Science Place, Saskatoon, Saskatchewan S7N 5E2, Canada
[b] Department of Earth Sciences, Laurentian University, 935 Ramsey Lake Road, Sudbury, Ontario P3E 2C6, Canada

ARTICLE INFO

Article history:
Received 17 February 2015
Received in revised form 20 July 2015
Accepted 23 July 2015
Available online 30 July 2015

Keywords:
Airborne electromagnetic
Dipole
Conductor
Energy Envelope
Total Component

ABSTRACT

This paper is a comparative study of the Energy Envelope and the *T*-component response for interpreting airborne electromagnetic (AEM) data. The Energy Envelope is the square root of the sum of squares of three component AEM data along with their Hilbert transforms, while the *T*-component response is a similar quantity, except without the Hilbert transform terms. These quantities can be used to determine approximate geometrical parameters of compact anomalous targets. The approximate parameters are useful for constraining automatic interpretation algorithms.

Synthetic examples are generated using a dipole conductor model. The synthetic models show that the Hilbert transform terms included in the Energy Envelope yield no additional benefits with regard to AEM data interpretation. Hence, the *T*-component response is a more efficient quantity for AEM modeling.

The position of the peak of the *T*-component response can be used to estimate the position of a compact target that is consistent with the measured response. In particular for a MEGATEM configuration and when the target lies directly below the flight line and the line spacing of the survey is 200 m, the error in predicting the position of the target is under 200 m. This error is improved in situations where the conductor is at an offset to the flight line, or when the line spacing is decreased. The strike of the conductor can also be estimated, as a series of peaks will align along the strike direction.

Once the position and strike of the conductor is known, look-up-tables are generated for these specific parameters. The look-up-tables can be used to determine the depth and dip of the target. The depth can be estimated from the full width at half magnitude of the *T*-component response. The dip can be estimated from the asymmetry of the *T*-component response.

Tests over the Chibougamau field site yield results in reasonable agreement with previous work of the same authors.

1. Introduction

Airborne electromagnetic (AEM) methods are an important tool in the exploration for mineral deposits (Vallée et al., 2011). Recent case history examples that focus on AEM methods are given by (Guo et al., in press; Legault, in press; Lymburner and Smith, 2015; Sattel, 2005; Yang et al., 2014). Methods to interpret and invert the data have recently been reviewed by Yin et al. (2015). Important models for interpretation of these data are the plate and the sphere models (Macnae et al., 1998; Schaa, 2010; Smith and Wasylechko, 2012; Vallée, 2015; Fullagar et al., in press).

AEM data is challenging to interpret as a result of the dependence on complex system geometry. This issue was addressed by Desmarais and Smith (accepted for publication-a), who devised an automatic interpretation algorithm capable of determining the geometrical parameters of a dipole conductor. However, the Desmarais and Smith (accepted for publication-a) algorithm can take several hours to run on the average personal computer, when sampling a large region of parameter space, if applied to large datasets. A more effective approach would consist of initially determining approximate parameters through forward modeling, prior to applying automatic interpretation algorithms. In this manner, a smaller region of parameter space would be investigated and computational resources could be greatly reduced.

Authors have suggested using the Hilbert (or Kramers–Kronig) transform for interpretation of potential field data acquired using the self-potential method (Akgün, 2001; Debeglia and Corpel, 1997) and the magnetic method (Bournas and Baker, 2001; Cooper, 2009; Nabighian, 1972, 1974, 1984). The Hilbert transform is a relation between the real and imaginary parts of a complex function known as the analytic signal. The real part of the analytic signal is the original data, the imaginary part is the Hilbert transform of the original data. The Hilbert transform follows directly from the properties of analytical

* Corresponding author at: Formerly Laurentian University.
E-mail addresses: jkd788@mail.usask.ca (J.K. Desmarais), RSSmith@laurentian.ca (R.S. Smith).

http://dx.doi.org/10.1016/j.jappgeo.2015.07.015
0926-9851/

functions (namely, the Cauchy–Riemann conditions and the Cauchy integral theorem), applied to the Fourier transform (Oppenheim et al., 1998).

Smith and Keating (1996) suggested interpreting electromagnetic data using an empirical quantity calculated the same way as the absolute amplitude of the analytic signal. They formed a quantity known as the Energy Envelope (EE). The EE is the square root of the sum of the squares of the three components and their three Hilbert transforms. This quantity is useful as it gives a single peak over a vertical conductor when calculated on the data acquired with an airborne EM system. The EE also shows some asymmetry for fixed-wing systems. This asymmetry is a consequence of the manner in which the asymmetric transmitter receiver system couples to the conductor. Normalizing the individual components by the EE can remove some of this asymmetry.

Mercer (2012) has proposed using the EE for generating maps of ground EM data. He argues that it generates a single peak anomaly over an anomalous body; whereas the individual components (in the *x*, *y* or *z* directions) show crossover anomalies or more complex features involving lows and highs. He also argued that the EE gave a sharper or narrower anomaly than the individual components or the *T*-component (The square root of the sum of the squared of the three individual components; i.e. the EE without the Hilbert transforms terms included).

Following the work of Mercer (2012), Desmarais and Smith, 2015b generated maps of the EE, the *T*-component response, as well as the *T*-component Hilbert transform response (the EE without the untransformed quantities), for the case of ground EM data. They showed that the *T*-component response and the EE generate peaks over a dipolar body, regardless of the orientation of this body. Thus, the position of the peak of the EE or the *T*-component response can be used to infer the position of the conductor. Once the position has been determined, other geometrical parameters such as the strike, dip and depth of the body can be extracted by combining the *T*-component and *T*-component Hilbert transform of the secondary magnetic field response (Desmarais and Smith, 2015b). In addition, Desmarais and Smith, 2015b showed that the *T*-component response is sharper in plan format than the EE for the majority of possible target orientations and is thus most useful to plot in plan format for locating the conductor.

Macnae (1984) showed that the response of a conductor excited by a fixed transmitter source is a potential field, in the quasi-static approximation. Thus, measurements obtained from ground EM systems are potential fields. In the case of potential fields, the EE is equivalent to the absolute amplitude of the analytic signal. In contrast, for the case of AEM systems where the transmitter is mobile, a profile of measurements is not a potential field, but rather a series of potential fields each generated from locally fixed transmitters. Consequently, it is expected that the manner in which the EE and *T*-component responses vary as a function of target geometry may differ from the findings of Mercer (2012) and Desmarais and Smith, 2015b, for the case of AEM systems.

In what follows, we generate examples to compare the EE and the *T*-component responses, and use these quantities to determine approximate geometrical parameters of compact anomalous targets for AEM surveys. We hope that this modeling approach will aid geophysical practitioners to determine approximate parameters in order to constrain automatic interpretation algorithms and regularize inversion algorithms.

2. Methodology

The synthetic models investigated in this study are generated using the dipole conductor formula of Desmarais and Smith (accepted for publication-a). A dipole is a good approximation to an inductively thin plate, which may be considered small relative to the distance between the body and the transmitter–receiver system (Desmarais and Smith, accepted for publication-a). Extension to more complex models including the effects of galvanic interactions, plate-like conductors of finite extent or higher order poles are not considered in this paper. We restrict our study to the case of a dipole–conductor model, as we seek to find a fully time-independent method for extracting the geometrical parameters of the conductor. Indeed, within the dipole approximation, the shape and relative amplitudes of the spatial components of the secondary-magnetic fields are not a function of time (Desmarais and Smith, accepted for publication-a). Only the absolute amplitudes of the spatial components change as a function of time. The manner in which the absolute amplitudes vary as a function of time depends on the body dimensions and its conductivity (Smith and Lee, 2001). As such, using a dipole conductor model, the geometrical parameters of the conductor may be extracted through modeling the response acquired along one channel and the effects of body dimensions and conductivity may be separated from those of the geometrical parameters. In this manner, we show that the geometrical parameters of the conductor can be extracted using the *T*-component response or the EE.

Consider now a physical model consisting of a compact plate-like conductor in free space (Fig. 1). The transmitter consists of an elevated vertical magnetic dipole. The free space dipolar field of the transmitter at the location of the target $\boldsymbol{F_{tot}}$ can be expressed as:

$$\boldsymbol{F_{tot}} = \frac{1}{4\pi r_{trtx}}\left[\frac{3\boldsymbol{m_{tx}}\cdot\boldsymbol{r_{trtx}}}{r_{trtx}^2}\boldsymbol{r_{trtx}} - \boldsymbol{m_{tx}}\right] \tag{1}$$

$$\boldsymbol{F_{tot}} = \left[F_x, F_y, F_z\right] \tag{2}$$

where $\boldsymbol{m_{tx}}$ is the magnetic moment of the transmitter vector, $\boldsymbol{r_{trtx}}$ is the vector offset from the target to the transmitter, r_{trtx} is the magnitude of $\boldsymbol{r_{trtx}}$, and $\cdot$ is the dot product operator. This formula is defined in a Cartesian coordinate system with its origin at the target (Fig. 1).

Then, the time-independent magnetic field response of the target measured at the location of the receiver $\boldsymbol{H}$ can be expressed as (Desmarais and Smith, accepted for publication-a):

$$\begin{aligned}\boldsymbol{H} = {} & \boldsymbol{R_x}F_x sin^2\theta sin^2\phi + (\boldsymbol{R_x}F_y + \boldsymbol{R_y}F_x) sin^2\theta sin\phi cos\phi \\ & + (\boldsymbol{R_x}F_z + \boldsymbol{R_z}F_x) sin\theta cos\theta sin\phi + \boldsymbol{R_y}F_y sin^2\theta cos^2\phi \\ & + (\boldsymbol{R_y}F_z + \boldsymbol{R_z}F_y) sin\theta cos\theta cos\phi + \boldsymbol{R_z}F_z cos^2\theta,\end{aligned} \tag{3}$$

where θ is the dip of the target and ϕ is the strike of the target. The dip is expressed in degrees below the horizontal over the interval $\theta \in (0, 90)$, and the strike is expressed in degrees from the traverse line in the clockwise direction over the interval $\phi \in (0, 180)$. The terms $\boldsymbol{R_i}$ are the fields

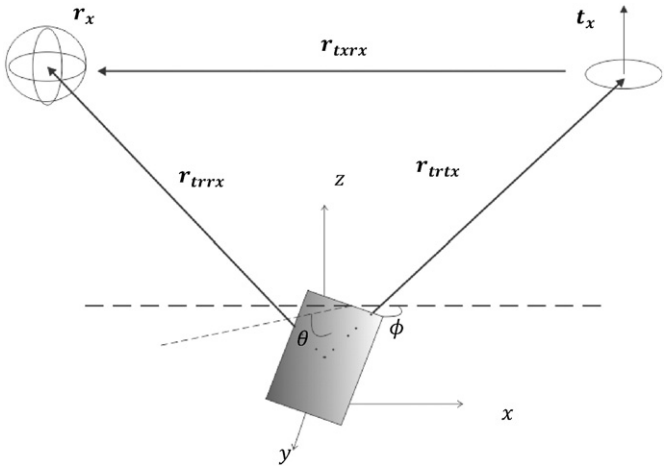

Fig. 1. Perspective diagram of the physical model of interest. The problem is defined in a Cartesian coordinate system with its origin at the center of the plate. The plate is oriented at a strike ϕ and a dip θ. The transmitter $\boldsymbol{t_x}$ is at a distance $\boldsymbol{r_{trtx}}$ from the plate, and is approximated as a vertical magnetic dipole. The three component receiver $\boldsymbol{r_x}$ is at a distance $\boldsymbol{r_{trrx}}$ from the target, and a distance $\boldsymbol{r_{rxtx}}$ from the transmitter.

produced from orthonormal unit dipoles located at the target:

$$\boldsymbol{R_x} = \frac{1}{4\pi r_{trrx}}\left[\frac{3[1,0,0]\cdot \boldsymbol{r_{trrx}}}{r_{trrx}^2}\boldsymbol{r_{trrx}} - [1,0,0]\right], \tag{4a}$$

$$\boldsymbol{R_y} = \frac{1}{4\pi r_{trrx}}\left[\frac{3[0,1,0]\cdot \boldsymbol{r_{trrx}}}{r_{trrx}^2}\boldsymbol{r_{trrx}} - [0,1,0]\right], \tag{4b}$$

$$\boldsymbol{R_z} = \frac{1}{4\pi r_{trrx}}\left[\frac{3[0,0,1]\cdot \boldsymbol{r_{trrx}}}{r_{trrx}^2}\boldsymbol{r_{trrx}} - [0,0,1]\right], \tag{4c}$$

and $\boldsymbol{r_{trrx}}$ is the vector offset from the target to the receiver.

3. Results

To generate the synthetic models, the AEM system is comprised of a vertical magnetic dipole transmitter flying along the x direction and towing a three-component receiver offset by 128 m in the x direction and 50 m (down) in the z direction. The target is positioned at 100 m depth in the center of the profile ($x = 0$) and at an offset of 1 m to the traverse line ($y = 1$). The 1 m offset is chosen to avoid null-coupling of the components of primary fields. The response is plotted at the x position of the receiver.

Fig. (2) shows a response computed using Eq. (3) for a synthetic model at a strike of 60° and a dip of 70°. As can be seen from the figure, this response has many peaks and troughs and it is difficult to accurately determine target properties based on visual inspection of the profiles.

The response can be simplified using the EE defined as (Smith and Keating, 1996):

$$\mathrm{EE} = \sqrt{H_x^2 + \tilde{H}_x^2 + H_y^2 + \tilde{H}_y^2 + H_z^2 + \tilde{H}_z^2}, \tag{5}$$

where H denotes a magnetic field measurement, the subscript denotes the spatial component, and the large tilde is the space-to-wavenumber-domain Hilbert transform operator. The space-to-wavenumber-domain Hilbert transform of a qth component measurement is expressed as:

$$\tilde{H}_q(k_x,k_y) = \frac{1}{\pi^2}\int_{-\infty}^{\infty}\frac{1}{k_x - r_x}dr_x\int_{-\infty}^{\infty}\frac{H_q(r_x,r_y)}{k_y - r_y}dr_y, \tag{6}$$

where r_x,r_y are spatial variables and k_x,k_y are the associated wavenumbers. This transformation is computed using the method outlined in Desmarais and Smith, 2015b. If data are plotted as plan maps, a 2 dimensional Hilbert transform is calculated. If data are plotted as profiles, a 1 dimensional Hilbert transform is calculated.

For the purposes of studying its properties, we decompose the EE into two parts:

$$\mathrm{EE}^2 = H_T^2 + \tilde{H}_T^2, \tag{7}$$

where H_T is the T-component response and $\tilde{H}_T$ the T-component Hilbert transform response:

$$H_T = \sqrt{H_x^2 + H_y^2 + H_z^2} \tag{8}$$

$$\tilde{H}_T = \sqrt{\tilde{H}_x^2 + \tilde{H}_y^2 + \tilde{H}_z^2}. \tag{9}$$

Fig. (3) is a plot of EE, H_T and $\tilde{H}_T$ for the same synthetic model associated with Fig. (2). As can be seen, the response is greatly simplified from Fig. (2) in all three cases. All three quantities in Fig. (3) generate a large peak near the anomalous body, so that they all provide viable options for plotting as plan maps or contours and determining the position of the body.

The manner in which the EE, H_T and $\tilde{H}_T$ vary as a function of strike and dip can be studied as follows. Firstly, we claim that the magnetic field response of a compact plate-like conductor in any arbitrary orientation can be expressed as a linear combination of the fields produced from unit dipoles oriented parallel to the [1, 0, 0], [0, 1, 0] and [0, 0, 1] directions. The linear combination of the field from unit dipoles is a simplification that is valid when the target dimensions are much smaller than the distance between the target and the transmitter–receiver system. For example, in the case of the sphere response, the first term corresponds to the dipole response, but higher order terms, which will be more important for larger radius spheres, are multipole fields which are more complex than dipole fields. It is also expected that for a plate response, the larger eigencurrents of Annan (1974) will generate fields of multipole nature, which cannot be described as a sum of the fields from unit dipoles. In summary, the claim that the magnetic-field response of a plate-like conductor can be expressed as a linear combination of fields produced by unit dipoles is only valid when source and

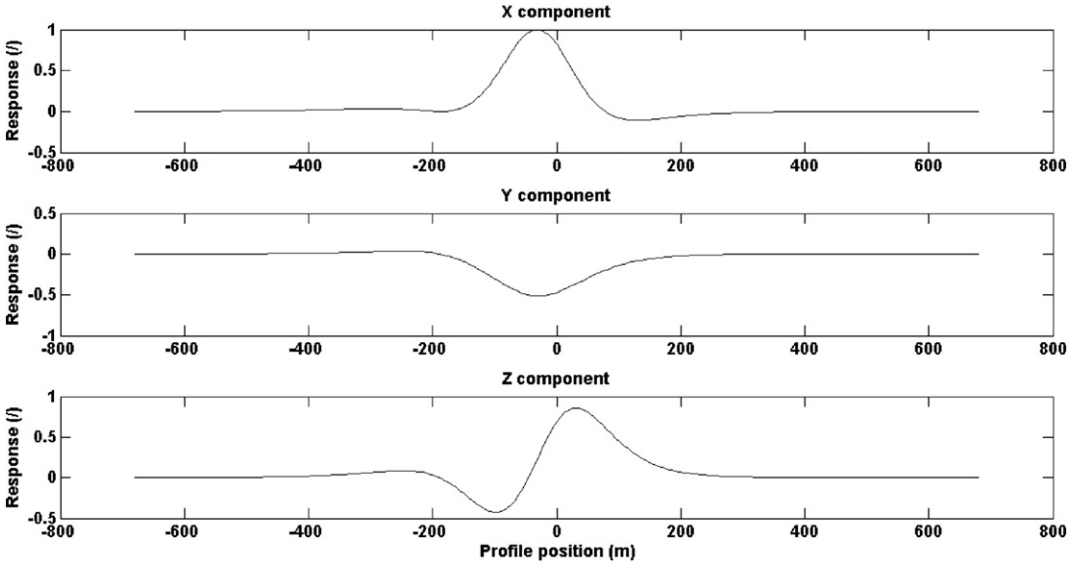

Fig. 2. Three component AEM response of a synthetic model at a strike of 60° and a dip of 70°. The response has many peaks and troughs and is complicated to interpret. The units of the response are arbitrary. The flight direction on this and subsequent figures is to the right.

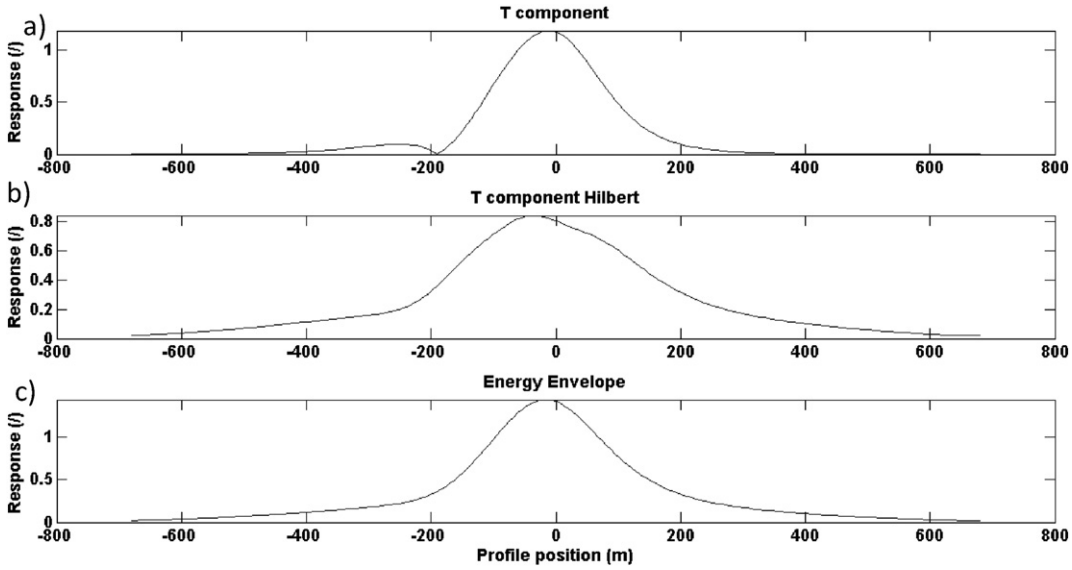

Fig. 3. (a) *T*-component response, (b) *T*-component Hilbert response and (c) Energy Envelope for the synthetic model at a strike of 60° and a dip of 70°. The response is greatly simplified from Fig. (2) in all three cases. The units of the response are arbitrary.

receiver distance are much larger than the dimensions of the target, in the way defined by Vallée (2015).

Fig. (4) is a plot of EE, H_T and $\tilde{H}_T$ for a synthetic model at a strike of 90° and a dip of 90° (dipole moment parallel to [1, 0, 0]), as well as a plan map view of these fields when five traverse lines are flown across the profile with a traverse line spacing of 200 m. As before, the profile views are plotted for the 0 m offset traverse line. The white dot indicates the position where the fields are a maximum. The gray dot indicates the location of the anomalous body. The gray dashed lines in Fig. (4d–f) shows the position of the traverse lines. The contour maps are white in some regions where the plotted quantities are not zero in the profile views, because the last contour on the maps corresponds to a value of 0.1 and not zero. Fig. (5) is a similar plot for a synthetic model at a strike of 0° and a dip of 90° (dipole moment parallel to [0, 1, 0]). Finally, Fig. (6) shows the equivalent plots for a synthetic model at a strike of 90° and a dip of 0° (dipole moment parallel to [0, 0, 1]).

The *T*-component response appears less broad than the Energy Envelope in Figs. (4), (5) and (6). As well, the *T*-component response is sharper than the Energy Envelope in plan format, making it more suitable for data interpretation. The *T*-component Hilbert transform response has a complicated shape, which is more difficult to interpret; hence it is excluded from the following discussion.

In all three cases, the position along the profile (position along the *x* axis of the figures) of the conductor is not exactly below the peaks of the EE and H_T. The peaks may be off by less than 100 m when the dipole moment is parallel to [0, 1, 0] or [0, 0, 1] (see solid black lines in Figs. 5 and 6).

The offset of the traverse line from the conductor is near the peaks of EE and H_T for the cases where the dipole moment of the target is oriented parallel to [1, 0, 0] and [0, 0, 1]. However, when the dipole moment is oriented parallel to [0, 1, 0], the peaks of EE and H_T are 200 m from the position of the conductor. This occurs because, when the dipole moment is oriented parallel to [0, 1, 0], the target strikes parallel to the traverse line and has a vertical dip, so that if it is directly under the traverse line (offset = 0 m) it will null couple with the transmitter. As the offset of the traverse line increases, the target is no longer null coupled with the transmitter, so that the *x*, *y* and *z* components of the response increase to a maximum value. In Fig. (5d), the maximum is reached at an offset of 200 m. When the offset continues to increase from 200 m, the distance from the target to the receiver becomes larger, so that the response begins to decrease.

The errors in predicting the offset from the traverse line of the conductor is greatly improved when the traverse line spacing is decreased. Fig. (7 a,b,c) show plan views of the *T*-component response for the cases where the dipole moments are parallel to the [1, 0, 0], [0, 1, 0] and [0, 0, 1] directions, respectively. This time, a similar simulation is performed except that a line spacing of 75 m was used instead of 200 m. As can be seen from Fig. (7a,b,c), the error in predicting the offset is now always below 100 m.

The errors in predicting the position of the conductor are also improved in situations where the target does not lie directly below one of the flight lines. Fig. (8 a,b,c) show plan views of the *T*-component response for the cases where the dipole moments are parallel to the [1, 0, 0], [0, 1, 0] and [0, 0, 1] directions, respectively. In this case, a simulation was performed with the original line-spacing of 200 m, however, the conductor is now placed at an offset of 50 m, instead of 1 m. Fig. (8) shows that for this situation, the error in predicting the offset of the conductor is now below 50 m.

To determine other geometrical parameters, we choose not to follow the approach of Smith and Keating (1996), who developed simple rules of thumbs to determine the geometry of the conductor. In fact, upon inspection of Eq. (3), it is clear that this equation is not separable with respect to the system parameters:

$$\boldsymbol{H}(\boldsymbol{r}_{\boldsymbol{trtx}}, \boldsymbol{r}_{\boldsymbol{trrx}}, \theta, \phi) \neq \boldsymbol{H}'(\boldsymbol{r}_{\boldsymbol{trtx}})\boldsymbol{H}'(\boldsymbol{r}_{\boldsymbol{trrx}})\boldsymbol{H}'(\theta)\boldsymbol{H}'(\phi), \tag{10}$$

where $\boldsymbol{H}$ is a three-dimensional secondary magnetic field measurement, as defined in Eq. (3) and $\boldsymbol{H}'$ is a decomposed version of this function, which does not exist. It is therefore not possible to develop individual relationships for each variable. Instead, our approach estimates the position and strike of the conductor from plan maps of the *T*-component response. The strike can be determined from the direction of elongation of the *T*-component response. This is not possible in our synthetic models, because our dipole conductor model does not represent an elongated body. However, when applied in field situations, an elongated body appears as a series of *T*-component peaks aligned in the strike direction or as a single asymmetric peak.

Once the strike and position of the conductor have been determined, the dip and depth can be estimated by comparing the field data with

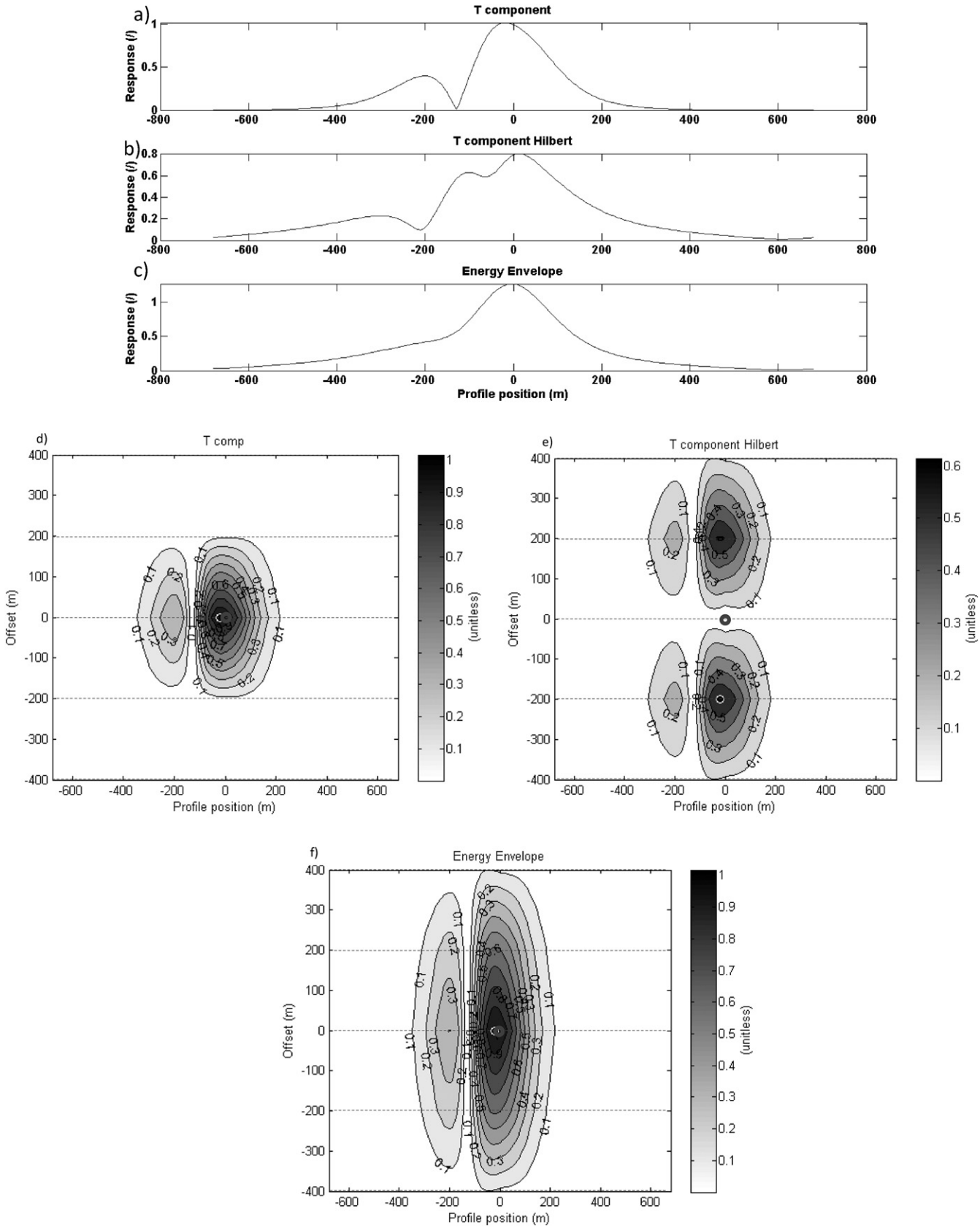

Fig. 4. (a) *T*-component response, (b) *T*-component Hilbert response and (c) Energy Envelope along profile, (d) *T*-component response (e) *T*-component Hilbert response and (f) Energy Envelope in plan view for the synthetic model at a strike of 90° and a dip of 90°. The dipole moment of the target is parallel to the [1, 0, 0] direction. The units of the response are arbitrary. The position of the compact conductor is shown with a gray circle and the position where the plotted quantities are a maximum is shown with a white circle on this and all subsequent figures.

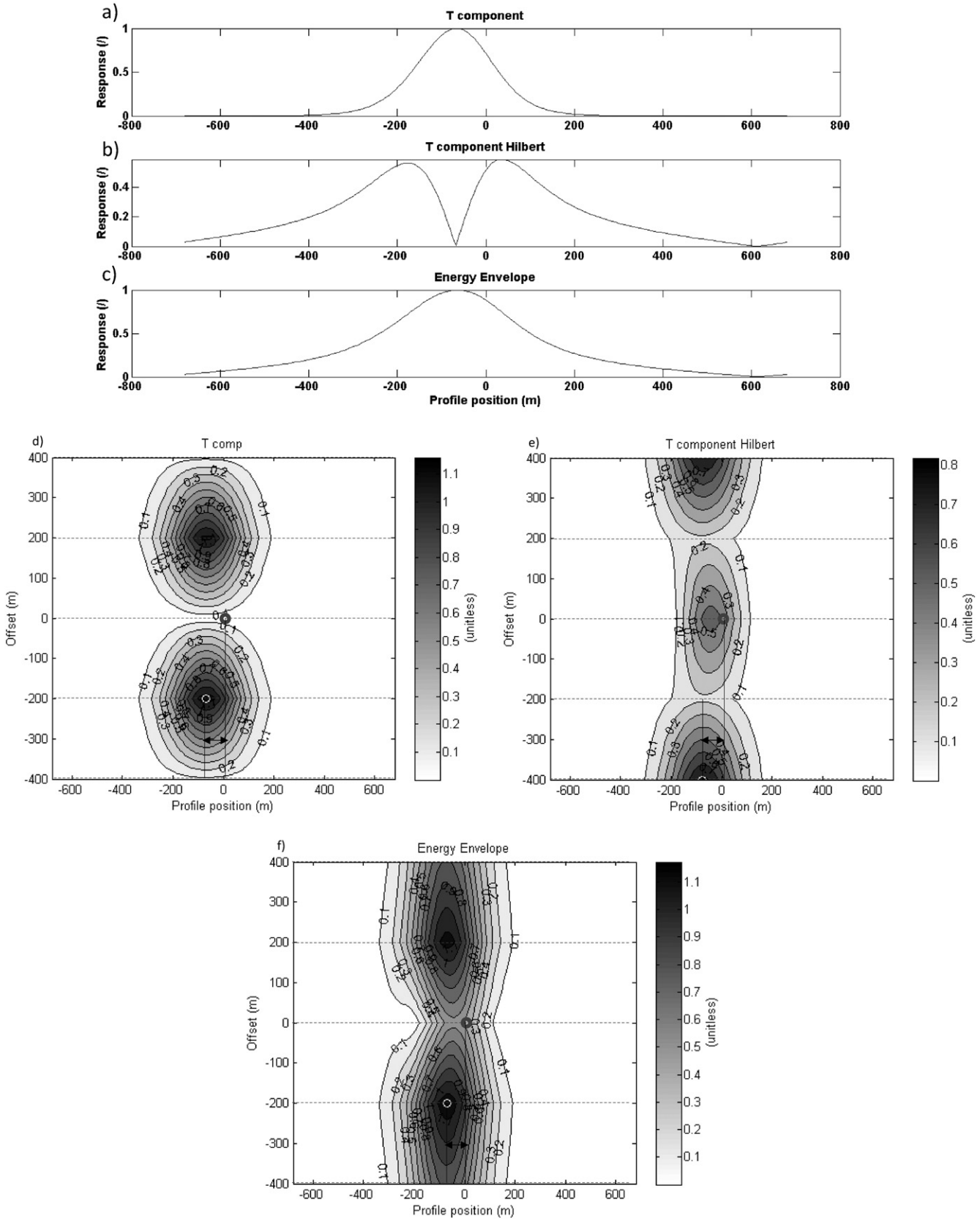

Fig. 5. (a) *T*-component response, (b) *T*-component Hilbert response and (c) Energy Envelope along profile, (d) *T*-component response (e) *T*-component Hilbert response and (f) Energy Envelope in plan view for the synthetic model at a strike of 0° and a dip of 90°. The dipole moment of the target is parallel to the [0, 1, 0] direction. The units of the response are arbitrary. The solid lines denote the position along the profile of the conductor and the maxima of the plotted quantities.

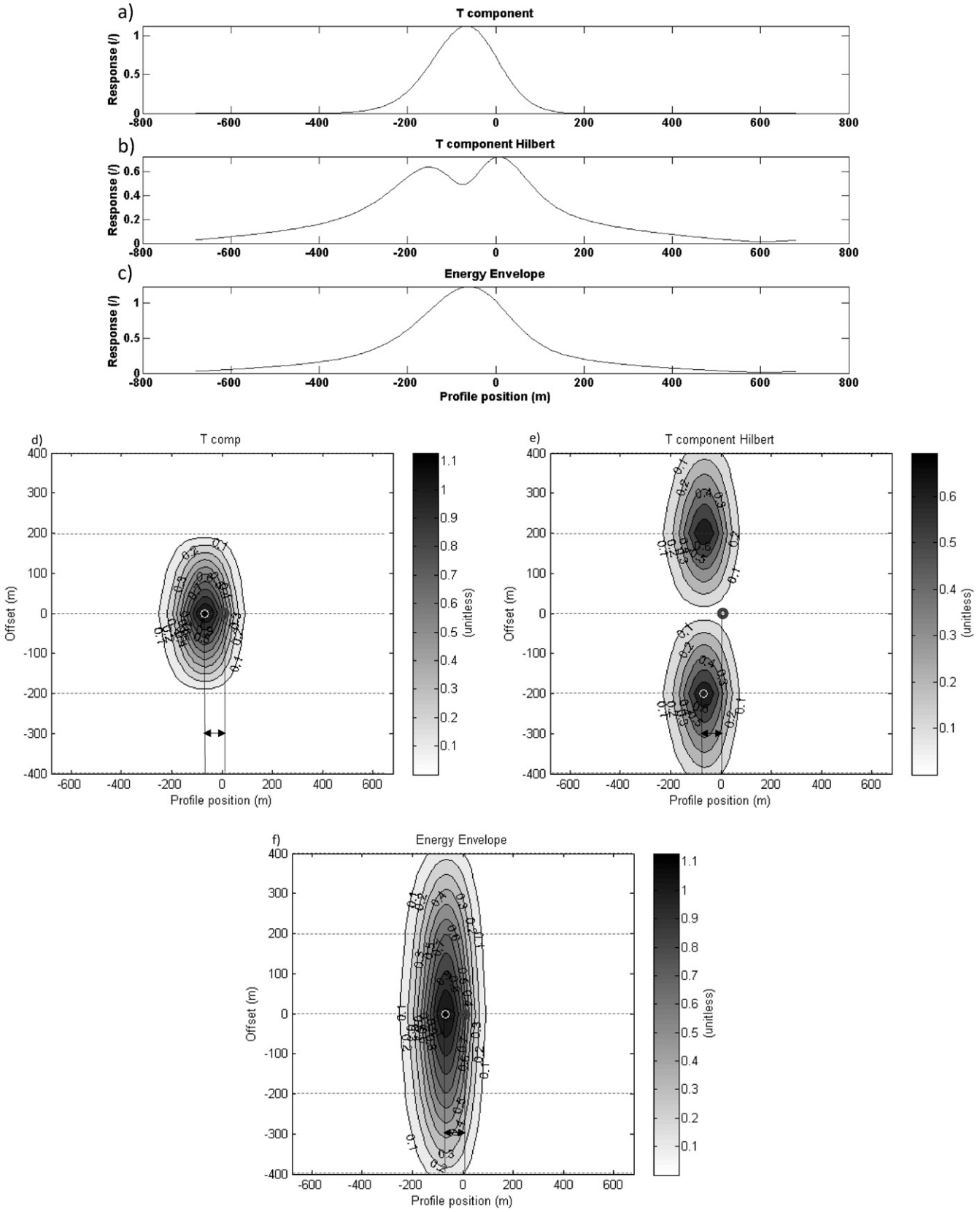

Fig. 6. (a) *T*-component response, (b) *T*-component Hilbert response and (c) Energy Envelope along profile, (d) *T*-component response (e) *T*-component Hilbert response and (f) Energy Envelope in plan view for the synthetic model at a strike of 90° and a dip of 0°. The dipole moment of the target is parallel to the [0, 0, 1] direction. The units of the response are arbitrary. The solid lines denote the position along the profile of the conductor and the maxima of the plotted quantities.

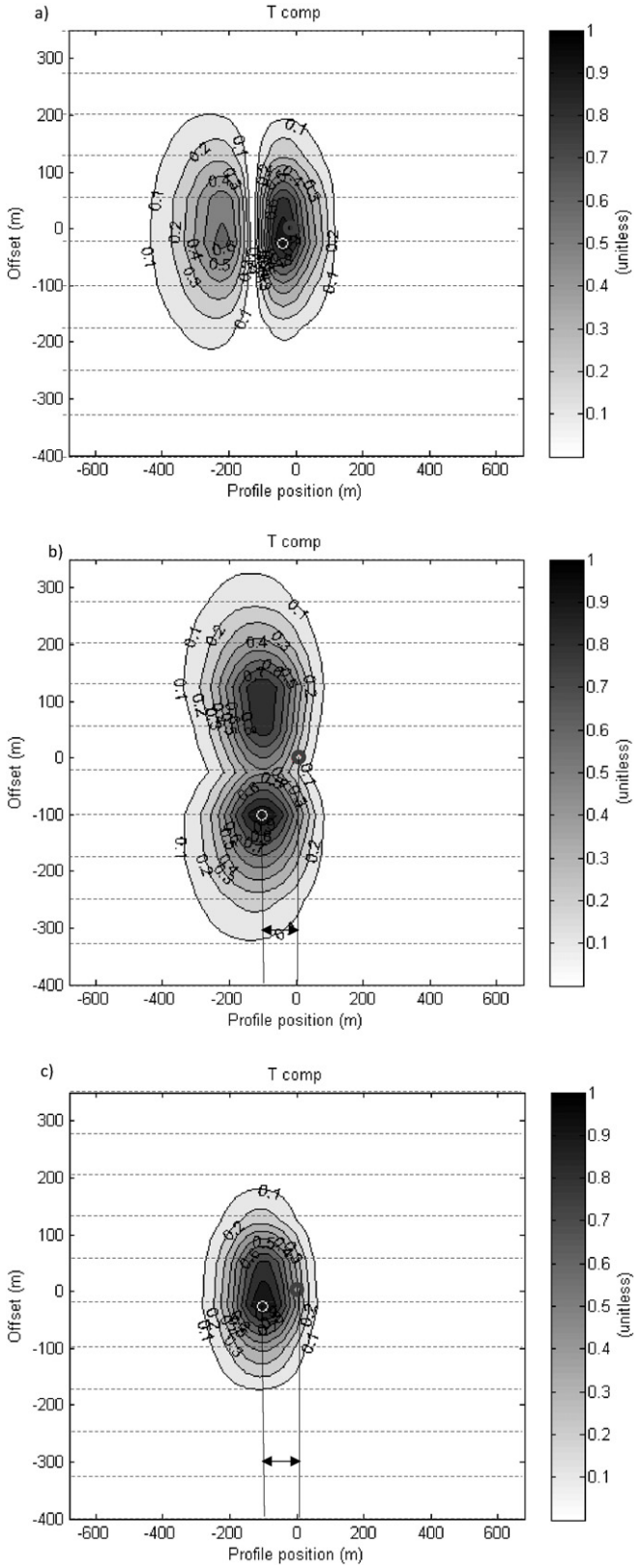

Fig. 7. *T*-component response for a simulation carried using a line spacing of 75 m instead of 200 m. The dipole moment of the target is parallel to the (a) [1, 0, 0] (b) [0, 1, 0] and (c) [0, 0, 1] directions. The errors in predicting the offset of the target is now below 100 m in all three cases. The units of the response are arbitrary. The solid lines denote the position along the profile of the conductor and the maxima of the plotted quantities.

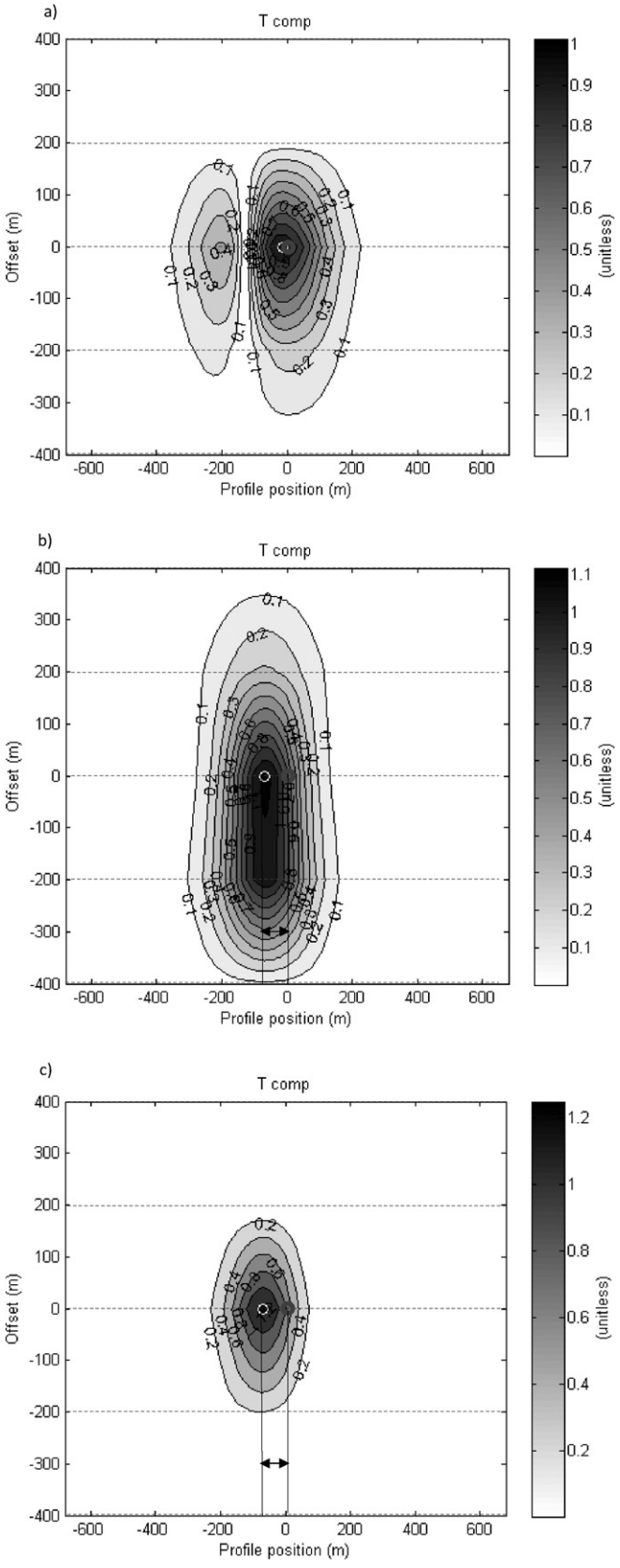

Fig. 8. *T*-component response for a simulation carried using the original line spacing of 200 m and a target placed at 50 m offset to the traverse line instead of 1 m. The dipole moment of the target is parallel to the (a) [1, 0, 0] (b) [0, 1, 0] and (c) [0, 0, 1] directions. The errors in predicting the offset of the target are now below 50 m in all three cases. The units of the response are arbitrary. The solid lines denote the position along the profile of the conductor and the maxima of the plotted quantities.

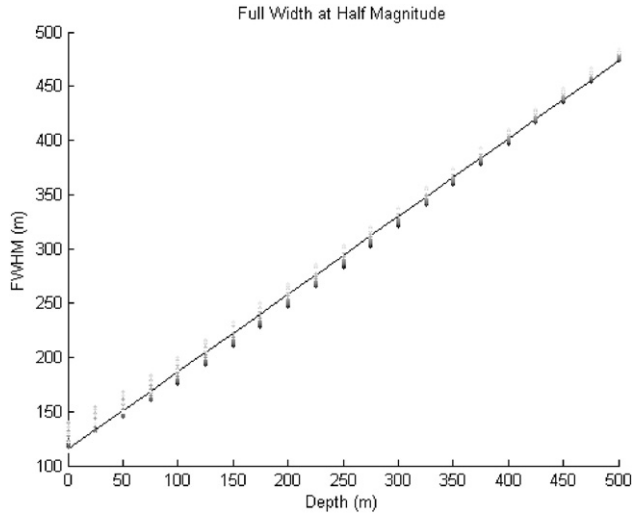

Fig. 9. Full width at half magnitude (FWHM) of the largest peak of the *T*-component response for a synthetic model at a position along the traverse line of 0 m, an offset to the traverse line of 0 m and a strike of 75°. Dark dots are plotted for low values of dip, whereas lighter dots are plotted for higher values of dip. The line of best fit has an intercept of 114.8985 m and a slope of 0.7167.

look-up-tables generated for the strike and position of interest. For example, Fig. (9) is a plot of the full width at half magnitude (FWHM) of the largest peak of the *T*-component response, as a function of depth. The plot was generated for a synthetic model at an offset of 0 m and a strike of 75°. The dark dots are plotted for lower values of dip, whereas the light dots are plotted for higher values of dip. The plot shows that for a given position and strike, the depth varies linearly with the FWHM regardless of the dip. The line of best fit has an intercept of 114.8985 m and a slope of 0.7167.

Once the depth has been determined from Fig. (9), the dip can be determined using one of the curves in Fig. (10) or one of the curves in Fig. (11). Fig. (10) is a plot of the normalized amplitude difference of the two peaks occurring in the *T*-component response, as a function of dip. Fig. (11) is a plot of the distance of separation of the two peaks in the *T*-component response, as a function of dip. For specific values of dip, the two plots have ambiguities, however the ambiguities occur in

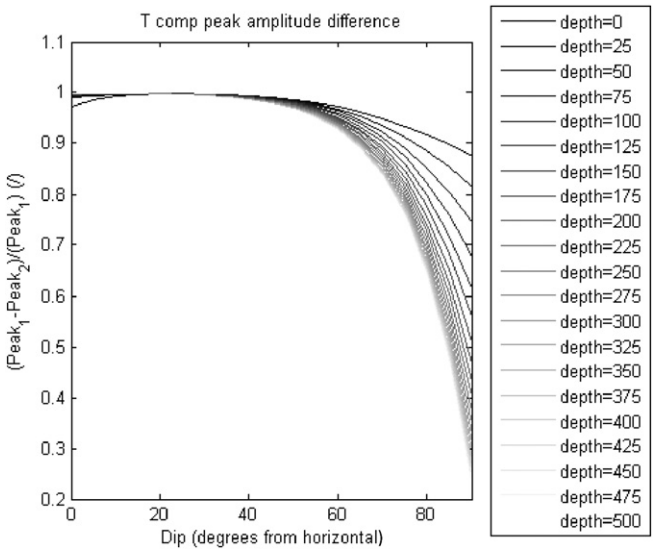

Fig. 10. Normalized peak magnitude difference as a function of dip for the two peaks occurring in the *T*-component response. One of the curves can be used to determine the dip, once the depth has been found using Fig. 9.

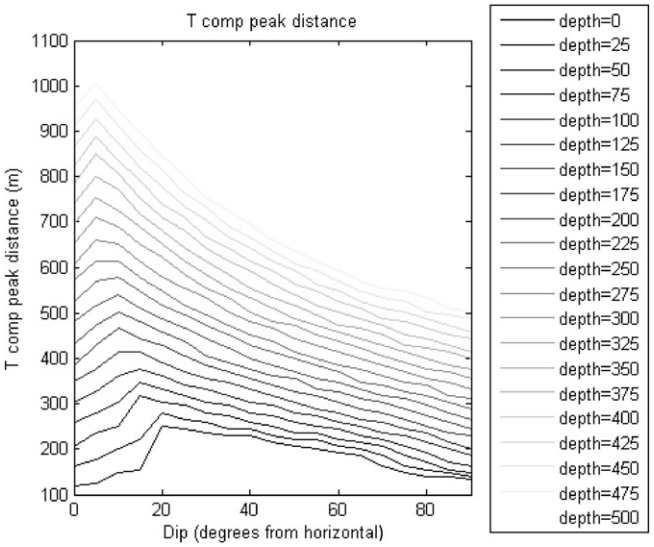

Fig. 11. Distance of separation as a function of dip for the two peaks occurring in the *T*-component response. One of the curves can be used to estimate dip, once the depth has been determined using Fig. (9).

different regions, so that the dip can be estimated from either of these two plots in most situations.

3.1. Test on field data over the Chibougamau test site

Our approach is tested on MEGATEM AEM data from lines 15301 to 15901 of the Chibougamau survey, Quebec. Desmarais and Smith (accepted for publication-a,b) discussed this same anomaly acquired over line 15701. The geometry of the AEM system is similar to the one used to generate the synthetic models. The line spacing for this survey was 200 m.

Fig. (12) is a plot of the *x*, *y* and *z* component responses acquired over these lines, as well as the associated *T*-component response the *T*-component Hilbert transform response and the Energy Envelope. The black dashed lines show the location of the traverse lines, which are labeled at the bottom of the figure. The units of the response are arbitrary. Comparing Fig. (12d), (e) and (f), it is evident that the sharper *T*-component response, is more suitable for interpretation than the Energy Envelope or the *T*-component Hilbert transform response.

Fig. (12d) shows a large anomalous feature striking at ~75°. This feature has many peaks which are centered about an axis denoted by the black solid line in Fig. (12d). The line is at an offset of 0 m and a transmitter position of approximately 5548 m relative to line 15701. The *T*-component anomaly along line 15701 has an FWHM of 206 m, a peak distance of 272 m and a normalized peak amplitude of 0.741. Using these parameters with the aid of Fig. (9) through (11), it is estimated that the conductor has a dip of 82.5° and a depth of 130 m. These parameters compare reasonably well with those of Desmarais and Smith (accepted for publication-a,b), who used the same dipole formula but fitted individual components using an automated procedure. The results of the analyses can be found in Table 1.

4. Discussion

The method presented herein uses a dipole conductor model. The dipole approximation assumes that the conductor's dimensions are small when compared to the distance from the body to the transmitter. Thus, our method is restricted to situations where the conductor of interest is relatively small. The extent of the validity of the dipole approximation for modeling large targets within the context of our implementation is not currently known. However, we decide to report on our findings in hopes of stimulating further research. We suggest that future work

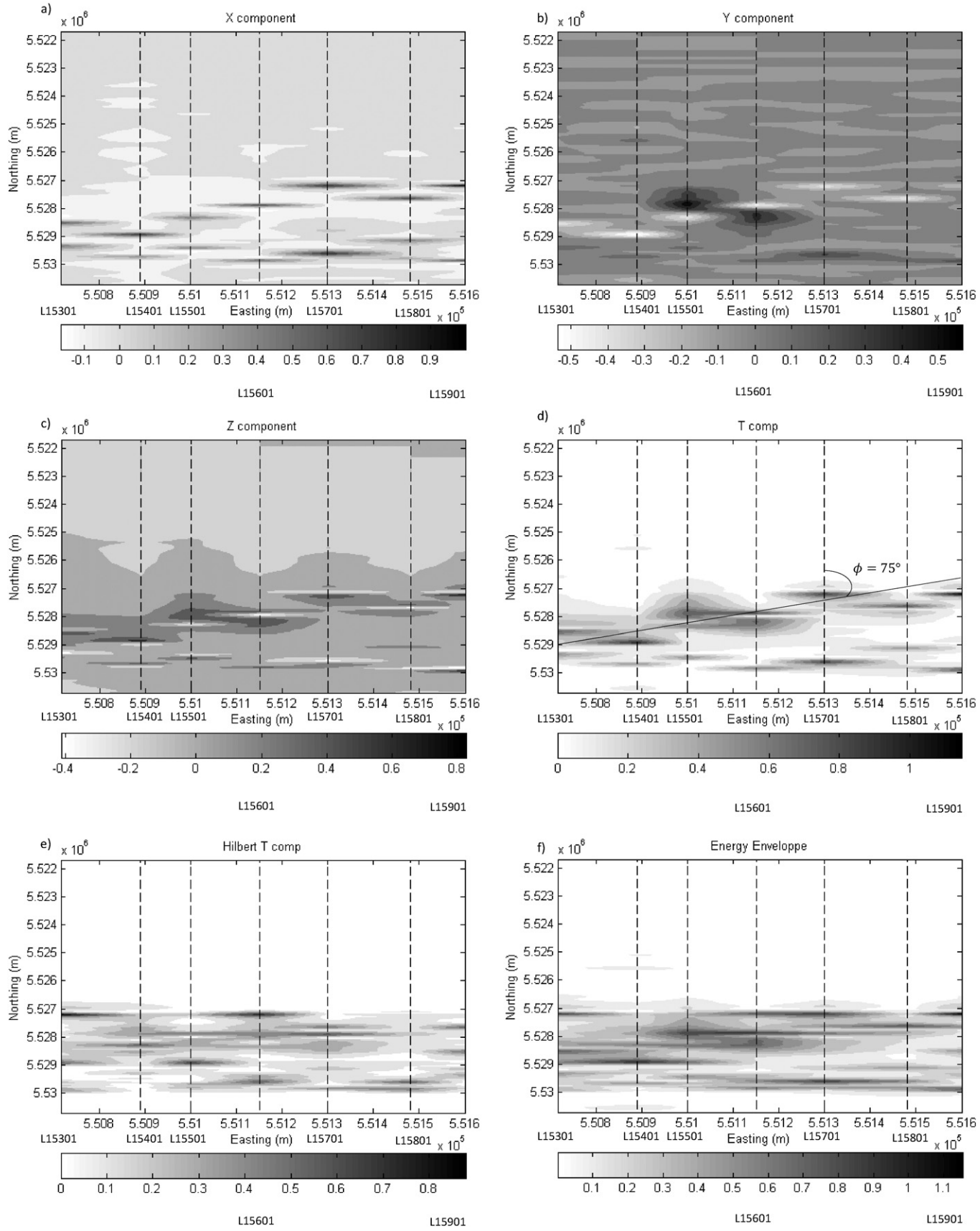

Fig. 12. (a) *x*-comp (b) *y*-comp (c) *z*-comp (d) *T*-comp (e) *T*-comp Hilbert, and (f) EE response at the Chibougamau field site. The black dotted lines show the location of the traverse lines, which are labeled at the bottom of the figure. Fig. 12(d) appears sharper than (e) or (f). The central axis of the *T*-component is denoted by the black solid line. Line L15701 is at an angle of approximately 75° to the central axis of the *T*-component. The units of the response are arbitrary.

Table 1
Comparison of the parameters obtained over the Chibougamau test site with those obtained by Desmarais and Smith (2015a) and Desmarais and Smith (2015b).

	Obtained parameters	Results of Desmarais and Smith (accepted for publication-a,b)
Dip	82.5°	80°
Strike	75°	65°
Position of the transmitter along traverse	5480 m	5555 m
Lateral offset	0 m	0 m
Depth below surface	130 m	175 m

investigate the effect of non-dipole targets, e.g. those with significant strike length and depth extent.

The proposed approach could be used by generating plots for both B field measurements or $\partial B/\partial t$ measurements. As previously outlined, within the dipole approximation the response shape is not a function of time (Desmarais and Smith, accepted for publication-a). As such, the response can be modeled at any arbitrary delay time. However, in practice it is recommended that the delay time yielding the largest signal-to-noise ratio be used for modeling. As discussed by Desmarais and Smith (2015a), B field measurements are most sensitive to highly conductive targets, while $\partial B/\partial t$ measurements are most sensitive to less conductive targets. The range of conductivity over which B field or $\partial B/\partial t$ measurements are most suitable depends on the shape of the transmitter current waveform. In practice, it is proposed that both B field and $\partial B/\partial t$ measurements are plotted as a T-component response and that the measurements yielding the greatest signal-to-noise ratio be used to extract the geometrical parameters of the target.

The response of the conductor responsible for the anomaly observed in the Chibougamau survey extends along several traverse lines. Considering that the dipole approximation works for only small conductors, it is possible that the Chibougamau conductor is too large to be represented within the dipole approximation. It is difficult to estimate whether or not a response is too broad to be modeled as a dipole conductor, as dipole conductors may generate broad responses if they are deep and have conductivity much larger than the background. If the Chibougamau conductor is too large to be represented by a dipole, the obtained depth and dip may be erroneous. Regardless of the accuracy of the obtained depth and dip, most importantly the results are in agreement with the automated interpretation of Desmarais and Smith (accepted for publication-a,b).

Estimating the position of the conductor from the position of the peaks of the T-component response and the EE does indeed introduce uncertainties. Therefore, we do not suggest that the proposed method be used to determine absolute geometrical parameters of a conductor. Rather, we propose that this method be used to generate approximate parameters which may be refined using more sophisticated algorithms, such as the algorithm of Desmarais and Smith (accepted for publication-a). For example, in the case of a MEGATEM configuration, our tests on synthetic models indicate that the errors in predicting the x and y positions of the conductor are below 200 m. Hence, the geometrical parameters could be refined using the Desmarais and Smith (accepted for publication-a) algorithm by searching the parameter space over $x \in (q - 200,\ q + 200)$; $y \in (p - 200,\ p + 200)$; $z \in (d_1,\ d_2)$; $dip \in (\theta_1, \theta_2)$; $strike = \phi$, where ϕ is the strike determined from the elongation of the T-component response; q and p are the x and y positions of the T-component response peak; d_1 and θ_1 are the depth and dip determined from plots similar to Figs. 9–11 for a conductor position of $[x, y] = [q - 200, p - 200]$ and a strike ϕ; d_2 and θ_2 are the depth and dip determined from plots similar to Figs. 9–12 for a conductor position of $[x, y] = [q + 200, p + 200]$ and a strike ϕ. As such, the search over the space of predicted parameters inherent to automated interpretation algorithms can be narrowed to a region of interest, reducing the computational time of automatic interpretation algorithms such as that of Desmarais and Smith (accepted for publication-a) by orders of magnitude. This decrease in computational time could allow for more complicated models (i.e. non-dipole models, models including galvanic interactions) to be implemented. Of course, if more complex models are implemented, plots similar to Fig. 9–11 would need to be recomputed using a modified version of Eq. (3).

5. Conclusion

The T-component response is more efficient than the Energy Envelope for interpreting AEM data. Not only is it less time consuming to calculate, it also appears sharper in plan format, as the Hilbert transform terms in the Energy Envelope tend to smear the data.

The shape of the T-component response can be used to determine approximate geometrical parameters of an anomalous conductor. The position of the peak of the T-component response can be used to determine the position of the conductor. The estimate is most accurate for conductors at an offset to the flight line, where the error does not exceed 50 m, for the specific flight line spacing, system and target geometry used. The strike of the conductor can also be estimated from the position of the peaks, as a series of peaks tend to align along the strike direction.

Once the strike and position of the conductor are known, look-up-tables can be generated for the pre-determined parameters in order to estimate dip and depth. The depth can be approximated from the full width at half magnitude of the T-component response. The dip can be estimated from the asymmetry of the T-component response.

Tests over the Chibougamau field site yield results in reasonable agreement with previous work of the same authors.

Acknowledgments

The authors would like to thank NSERC for giving a USRA to JKD. We would also like to acknowledge the assistance of Jean Lemieux and Brenda Sharp formerly of CGG Ottawa in directing us to appropriate geophysical and geological information.

References

Akgün, M., 2001. Estimation of some bodies parameters from the self potential method using Hilbert transform. J. Balkan Geophys. Soc. 4 (2), 29–44.
Annan, A.P., 1974. The Equivalent Source Method for Electromagnetic Scattering Analysis and Its Geophysical Application PHD thesis Memorial University of Newfoundland.
Bournas, N., Baker, H.A., 2001. Interpretation of magnetic anomalies using the horizontal gradient of the analytical signal. Ann. Geofis. 44 (3), 05–26.
Cooper, G.R.J., 2009. Balancing images of potential-field data. Geophysics 74 (3), 17–20.
Debeglia, N., Corpel, J., 1997. Automatic 3-D interpretation of potential field data using analytic signal derivatives. Geophysics 62 (1), 87–96.
Desmarais, J.K., Smith, R.S., 2015a. Survey design to maximize the volume of exploration of the InfiniTEM system when looking for discrete targets. J. Appl. Geophys. 115, 11–23.
Desmarais, J.K., Smith, R.S., 2015b. Combining spatial components and Hilbert transforms to interpret ground-time-domain electromagnetic data. Geophysics 80 (4), E237–E246.
Desmarais, J.K., Smith, R.S., 2015. Decomposing the electromagnetic response of magnetic dipoles to determine the geometrical parameters of a dipole conductor. Explor. Geophys. (accepted for publication-a).
Desmarais, J.K., Smith, R.S., 2015. The benefits of using multicomponent-transmitter–receiver systems for determining the geometrical parameters of a dipole conductor. Explor. Geophys. (accepted for publication-b).
Fullagar, P.K., Pears, G.A., Reid, J.E., Schaa, R., 2015. Rapid approximate inversion of airborne TEM. Explor. Geophys. http://dx.doi.org/10.1071/EG14046 (in press).
Guo, K., Mungall, J.E., Smith, R.S., 2013. The ratio of B-field and dB/dt time constants from time-domain electromagnetic data: a new tool for estimating size and conductivity of mineral deposits. Explor. Geophys. http://dx.doi.org/10.1071/EG13042 (in press).
Legault, J.M., 2015. ZTEM and VTEM airborne EM and magnetic results over the Lalor copper–gold VMS deposit region, near Snow Lake, Manitoba. Interpretation (in press).
Lymburner, J., Smith, R.S., 2015. A procedure for collecting electromagnetic data using multiple transmitters and receivers capable of deep and focussed exploration. Geophysics 80 (1), E1–E10. http://dx.doi.org/10.1190/geo2014-0251.1.
Macnae, J.C., 1984. Survey design for multicomponent electromagnetic systems. Geophysics 49 (3), 265–273.
Macnae, J., King, A., Stolz, N., Osmakoff, A., Blaha, A., 1998. Fast AEM data processing and inversion. Explor. Geophys. 29, 163–169. http://dx.doi.org/10.1071/EG998163.

Mercer, A., 2012. Combining Multiple Components of InfiniTEM Electromagnetic Data to Better Represent Subsurface Anomalies MSc thesis Memorial University of Newfoundland.
Nabighian, M.N., 1972. The analytical signal of two-dimensional magnetic bodies with polygonal cross-section: Its properties and use for automated anomaly interpretation. Geophysics 37 (3), 507–517.
Nabighian, M.N., 1974. Additional comments on the analytic signal of two-dimensional magnetic bodies with polygonal cross- section. Geophysics 39 (1), 85–92.
Nabighian, M.N., 1984. Toward the three- dimensional automatic interpretation of potential field data via generalized Hilbert transforms: fundamental relations. Geophysics 49 (3), 780–786.
Oppenheim, A.V., Schafer, R.W., Buck, J.R., 1998. Discrete-time Signal Processing. Prentice Hall, Upper Saddle River, New Jersey.
Sattel, D., 2005. Inverting airborne electromagnetic (AEM) data with Zohdy's method. Geophysics 70, G77–G85.
Schaa, R., 2010. Rapid Approximate 3D Inversion of TEM Data Ph.D. thesis University of Tasmania.
Smith, R.S., Keating, P.B., 1996. The usefulness of multicomponent, time-domain airborne electromagnetic measurements. Geophysics 61, 74–81.
Smith, R.S., Lee, T.J., 2001. The impulse-response moments of a conductive sphere in a uniform field, a versatile and efficient electromagnetic model. Explor. Geophys. 32, 113–118.
Smith, R.S., Wasylechko, R., 2012. Sensitivity cross-sections in airborne electromagnetic methods using discrete conductors. Explor. Geophys 43, 95–103.
Vallée, M.A., 2015. New developments in AEM discrete conductor modelling and inversion. Explor. Geophys. http://dx.doi.org/10.1071/EG14025.
Vallée, M.A., Smith, R.S., Keating, P., 2011. Metalliferous mining geophysics — state of the art after a decade in the new millennium. Geophysics 76, W31–W50.
Yang, D., Oldenburg, D.W., Haber, E., 2014. 3-D inversion of airborne electromagnetic data parallelized and accelerated by local mesh and adaptive soundings. Geophys. J. Int. 196, 1492–1507.
Yin, C.C., Ren, X.Y., Liu, Y.H., Qi, Y.F., Qiu, C.K., Cai, J., 2015. Review on airborne EM inverse theory and applications. Geophysics 80 (4), W17–W31.